LANGMUIR

pubs.acs.org/Langmuir Article

Understanding the Strength of the Selenium—Graphene Interfaces for Energy Storage Systems

Vidushi Sharma, David Mitlin,* and Dibakar Datta*



Cite This: https://dx.doi.org/10.1021/acs.langmuir.0c02893



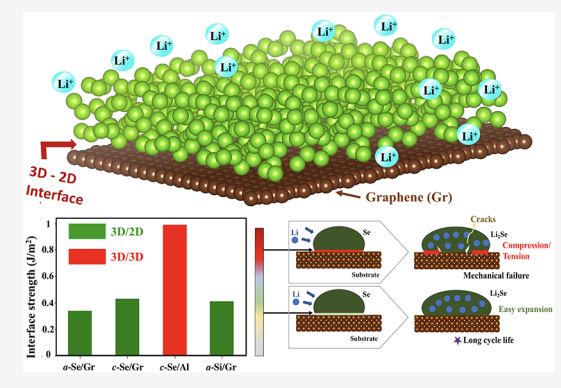
ACCESS

Metrics & More

Article Recommendations

Supporting Information

ABSTRACT: We present comprehensive first-principles density functional theory (DFT) analyses of the interfacial strength and bonding mechanisms between crystalline and amorphous selenium (Se) with graphene (Gr), a promising duo for energy storage applications. Comparative interface analyses are presented on amorphous silicon (Si) with graphene and crystalline Se with a conventional aluminum (Al) current collector. The interface strengths of monoclinic Se (0.43 J m⁻²) and amorphous Si with graphene (0.41 J m⁻²) are similar in magnitude. While both materials (c-Se, a-Si) are bonded loosely by van der Waals (vdW) forces over graphene, interfacial electron exchange is higher for a-Si/graphene. This is further elaborated by comparing the potential energy step and charge transfer (Δq) across the graphene interfaces. The interface strength of c-Se on a 3D Al current collector is higher (0.99 J m⁻²), suggesting a stronger adhesion. Amorphous Se with graphene has comparable interface strength (0.34 J m⁻²), but electron exchange in this



system is slightly distinct from monoclinic Se. The electronic characteristics and bonding mechanisms are different for monoclinic and amorphous Se with graphene as they activate graphene via surface charge doping divergently. The implications of these interfacial physicochemical attributes on electrode performance have been discussed. Our findings highlight the complex electrochemical phenomena in Se interfaced with graphene, which may profoundly differ from their "free" counterparts.

■ INTRODUCTION

The development of "next-generation" electrodes by combining materials into composite structures is gaining attention to enhance the energies and power-densities of existing ion battery technologies. Two or more materials are amalgamated in varied nano- and microstructures, where each component can contribute in one or many ways as an active electrode, ^{1,2} a composite additive and a binder, ^{3–10} a porous matrix, ¹¹ or even a current collector. ^{12,13} However, much less focus has been directed toward the interface chemistry of these materials. To this end, silicon (Si) is an exemplar anode where issues of cycle life, capacity, volume expansion, and surface reactivity have been successfully addressed by nanoengineering strategies such as Si alloys, ¹⁴ Si film composites, ¹⁵ Si -carbon (C) nanoparticle composites, ¹⁶ and porous Si mixed with carbon-based nanostructures. ¹⁷ Naturally, the interface of materials in such systems becomes the focal point, which dictates their applicatory success.

To match with high-specific-capacity (3000 mAh g⁻¹) anodes such as alloying Si, cathodes targeting high capacities and long battery cycles need further improvements. An elemental sulfur (S) cathode can deliver a high specific capacity of 1675 mAh g⁻¹ with its projected energy density being 2 to 3 times higher than conventional cathodes. However, having the primary concern of shuttle effects due to dissolution of Li–S reaction intermediates, 20-22 S is being

replaced by heavier chalcogens such as selenium (Se). $^{23-26}$ Li–Se cathodes are favored replacement for Li–S as Se possesses superior electrical conductivity (1×10^{-3} S m $^{-1}$ for Se and 5×10^{-28} S m $^{-1}$ for S) 27 and lithiation rates. 28 Li–Se cathodes have reported good gravimetric capacity (678 mAh g $^{-1}$) and very high volumetric capacity (3253 mAh cm $^{-3}$). 29,30 Since Se is a comparatively heavy and less reactive element than S, 31 shuttle effects in Li–Se cathodes due to dissolution of polyselenides are much controlled, if not negated. Furthermore, Se is capable of moving battery technologies a step further toward sustainable sodium-ion batteries with better sodiation kinetics. 32 This makes Se an ideal cathode candidate for next-generation energy storage materials.

Chalcogens directly react with Li/Na to undergo a conversion-type reaction accompanied by shuttle effects and significant volume expansions causing chemomechanical degradation. To overcome these, micro- and mesoporous C has been used as an additive to Se.³³ The porous matrix of C

Received: October 2, 2020 Revised: January 17, 2021



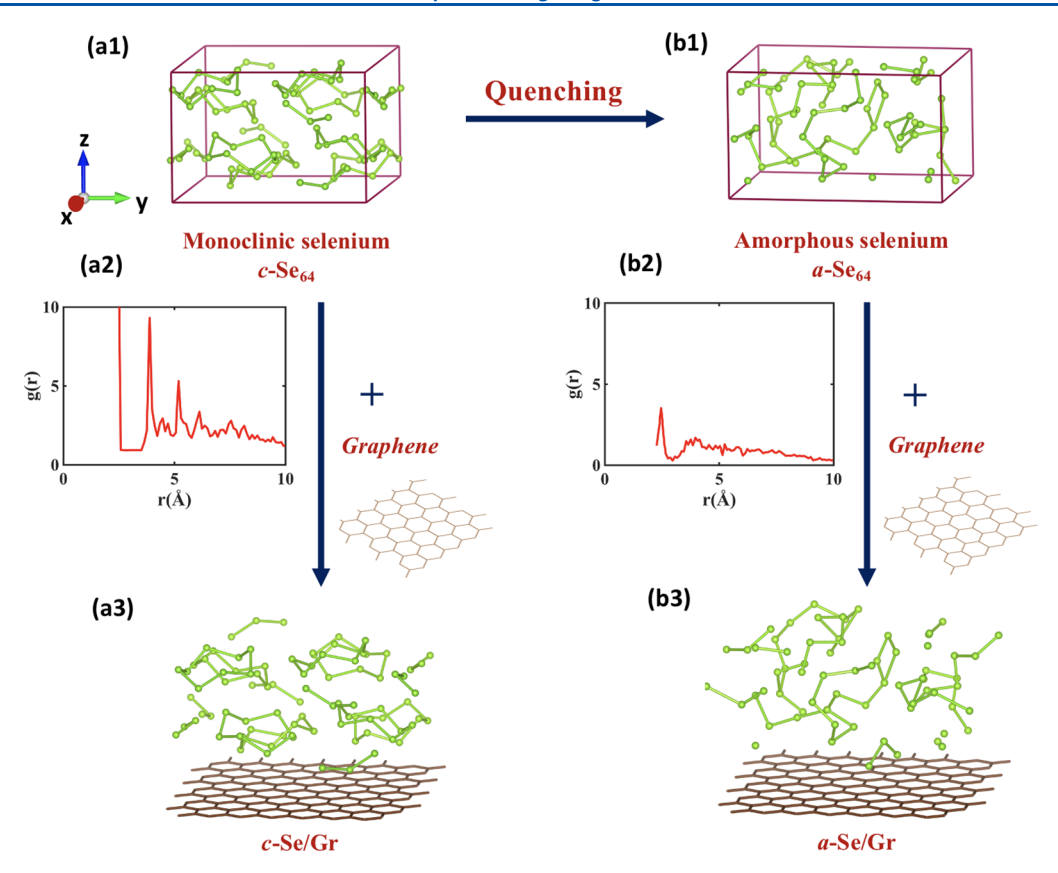


Figure 1. Schematic illustration of the quenching process to generate initial Se structures. (a1) Optimized monoclinic Se (c-Se) having Se₈ rings. (b1) Optimized amorphous Se (a-Se) generated from a monoclinic crystalline Se (c-Se) with computational quenching. The structure is dominated by disintegrated forms of Se rings. (a2) Radial distribution function (RDF) plot for monoclinic Se (c-Se) with the nearest neighboring distance of ~2.4 Å. More than one prominent peak is symbolic of crystallinity. (b2) RDF plot for amorphous Se (a-Se) obtained after quenching of monoclinic Se. The nearest neighboring distance is ~2.38 Å, and only one prominent peak is noted with low intensity. RDF plots for c-Se and a-Se conform and differentiate the structures of optimized Se allotropes. (a3) Representation of the initial structure of the c-Se/graphene interface prior to the interface study. (b3) Representation of the initial structure of the a-Se/graphene interface.

provides a buffer space for the active electrode Se to expand at ease, maintaining the continuity of electronic contact. In return, electronegative Se with its large pool of d electrons and polarizability manipulates the surface chemistry of the embedded C matrix and activates it to provide additional Li storage sites. 31,33-35 This affinity between the two materials also successfully suppresses the dissolution of polyselenides.³⁶ As the experimental techniques to infuse Se into C and resultant microstructures are varied, the electrochemical outcome of the Se-C cathode is impacted significantly. The electrochemical activity and cycle life of Se-C improve when morphology of C is shifted toward more refined nanostructures such as nanofibers, 35 carbon nanotubes, 36 and graphene. 37-39 Therefore, in the latest studies, porous C is now being replaced by graphene in Se-C systems. Being a 2D derivative of graphite, the most commercialized anode of LIB, graphene independently retains competence to store Li/Na. 1,2 This is evident in an experimental work by Han et al. 40 in which Se nanoparticles embedded in a mixture of mesoporous C and graphene, exhibited better discharge capacities and cycle life as LIB cathodes than Se in porous C alone.

Now that the electrochemical promise of graphene-based composite electrodes is nearly established, the greater challenge lies in characterizing the interface between graphene and the active electrode material. In a recent experimental and computational study on Si over the graphene substrate by Basu et al., ¹² slipperiness of the graphene surface proved to be

effective in combating stresses in the Si anode upon lithiation, thereby increasing the cycle life of the electrode. Interface adhesion between Si and the substrates was the primary determinant of electrode cycle life. While many prior studies claim that high adhesion between the active electrode material and additive will be beneficial for battery cyclability, 41–43 this study proves that low interface adhesion due to the slippery graphene surface could be instead more favorable for the battery life. A latest report 44 suggested that high interface strength between two materials can cause formation of structurally disconnected aggregates within the electrode. This condition could be avoided if the interface strength between two materials is carefully adjusted along with the other physicochemical factors.

To this end, the present study theoretically investigates the interface between 3D/2D Se/graphene. Se-graphene-based works are still in their infancy, with most of them being experimental reports. The atomic-level detailed investigation of the Se-graphene interface in terms of interfacial strength, bonding, and overall electronic character can benefit the systems utilizing Se-graphene such as in ion batteries and solar cells. We also present a comparative investigation of the amorphous Si-graphene interface as its efficacy is well utilized in batteries and can act as a baseline in this work. The novelty of the present study is that we have determined differences in the interface strengths of monoclinic and amorphous Se with the 2D hexagonal lattice of graphene. Se

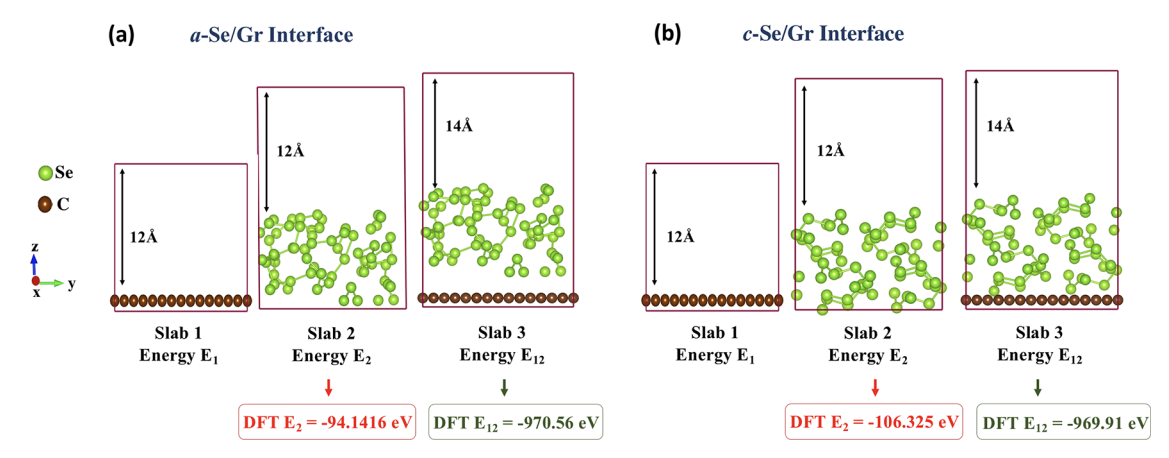


Figure 2. Vacuum interface models with three slabs taken for the work of separation calculations. (a) Three slabs taken for surface energy calculations of the amorphous Se and Gr interface (a-Se/Gr). (b) Three slabs taken for surface energy calculations of the monoclinic Se and Gr interface (c-Se/Gr). A vacuum of 12 Å was added in the z direction for slabs 1 and 2, 14 Å vacuum in the z direction for the slab 3 supercell containing the interface. E_2 for a-Se is higher than that for c-Se denoting the lower thermodynamic stability of the amorphous Se phase. The E_{12} of both the interface systems (c-Se/Gr and a-Se/Ge) is almost the same.

comes in several allotropic forms: monoclinic, trigonal, and amorphous. Being temperature- and pressure-sensitive, it undergoes phase transformations during its applications which remain less understood due to the marginal difference between structures of its different allotropes. Nevertheless, even these marginal structural changes in Se cause fluctuations in interface strength, bonding, the directionality of electron flow, and potential gradient at Se-based interfaces. Furthermore, these characteristics also influence the electronic states of Se and graphene distinctively, which we have investigated in detail using the density of states (DOS) analysis. Last, we discuss the prospective consequences of our interface analysis on the application of Se—graphene systems in batteries.

■ MATERIALS AND METHODS

The crystalline (c-) and amorphous (a-) phases of Se were modeled (Figure 1) before the interface analysis. Monoclinic Se with eightmembered monomer rings S₈ was opted as c-Se. The latter has structural parameters such as interatomic bond lengths, bond angles, and dihedral angles similar to its other crystalline allotropes. 46 Starting from c-Se, amorphous selenium (a-Se) was derived by computational quenching. 47,48 The quenching process required ab initio molecular dynamics (AIMD) within the DFT framework in the Vienna Ab initio Simulation Package (VASP).⁴⁹ We performed systematic heating, cooling, and equilibration of Se for 5000 MD time steps with a 1 fs time interval under the NVT canonical ensemble. The highest temperature considered (5000 K) was far above the melting point of Se. The final amorphous structure was obtained via DFT optimization of the room-temperature AIMD-simulated lowest-energy (local minima) structure. Projector-augmented-wave (PAW) potentials were used to mimic inert core electrons, while the valence electrons were represented by the plane-wave basis set. 50,51 The plane-wave energy cutoff and convergence tolerance for all relaxations were 550 and 1.0×10^{-6} eV, respectively. The GGA with the PBE exchangecorrelation function was taken into account. 52 For optimizing the initial structures of bulk c-Se and a-Se, gamma-centered $4 \times 4 \times 4$ kmeshes were employed for good convergence. Energy minimization was done by the conjugate gradient method with Hellmann–Feynman forces less than 0.02 eV ${\rm \AA}^{-1}$. The final c-Se and a-Se phases were identified using radial distribution function (RDF) plots. The RDF plot for c-Se in Figure 1a2 presents more than one prominent peak which is symbolic of crystallinity. Here, the nearest Se–Se distance of \sim 2.4 Å is noted. In contrast, the RDF plot in Figure 1b2 for a-Se exhibits the nearest Se-Se distance of \sim 2.38 Å and only one prominent peak with low intensity. These Se structures were then

interfaced with graphene (Gr) for further analysis (depicted in Figure 1a3,b3).

Investigation of interface strength requires surface energies of individual materials and energies of their interface systems. For surface energy calculation, material slabs with an added vacuum of 12 Å in the z dimensions were subjected to DFT. For interfaced systems, the vacuum interface model 53 with an added vacuum of 14 Å in the zdimensions (normal to the graphene plane) was used to calculate the interface energies (illustrated in Figure 2). In total, we studied three Se interface systems: 3D/2D (a- and c-)Se₆₄/Gr and 3D/3D c-Se₆₄/Al for comparison. In addition to Se, physicochemical characterization of the 3D/2D a-Si₆₄/Gr interface is also presented for correspondence. The choice of the Si/Gr interface for semblance is based on its wide utilization in lithium-ion battery systems. 3-7,12 With several interfacefocused analyses in light, the Si/Gr interface is a better alternative to validate our computational findings on 3D/2D interfaces with previous experimental understandings. In the present configuration, the number of Se or Si atoms in bulk is 64. For Se-Gr interface systems, Gr is composed of 112 sp² carbon atoms arranged in a hexagonal lattice, which takes into account the surface area of the c-Se₆₄ crystal in the (001) direction. Preparation of the a-Si/Gr interface system was reported previously 12 with the number of carbon atoms reduced to 60. In the c-Se₆₄/Al system, monoclinic Se₆₄ was interfaced with four atomic layers of Al as the substrate. These structures are periodic in the x-y dimensions. For DFT calculations of the vacuum models, gamma-centered $4 \times 4 \times 1$ k-meshes were employed and the GGA functional was inclusive of the vdW correction to incorporate the effect of weak long-range van der Waals (vdW) forces.⁵⁴ All calculations were done with the optPBE functional within the vdW-DF-family. 55,56

■ RESULTS AND DISCUSSION

Interface Strength Analysis. To evaluate the strength of Se–Gr interfaces, we first computed the work of separation $(W_{\rm sep})$ for each interface system. By definition, it is the energy per unit area required to separate the two materials completely in the direction normal to the interface. To accomplish this, slab models for (a-/c-) Se/Gr were created with vacuum in the z dimension to permit atomic relaxation and circumvent the periodic influence, as shown in Figure 2a,b. The standard description of $W_{\rm sep}$ is as follows

$$W_{\text{sep}} = \sigma_1 + \sigma_2 - \gamma_{12} = \frac{E_1 + E_2 - E_{12}}{A} \tag{1}$$

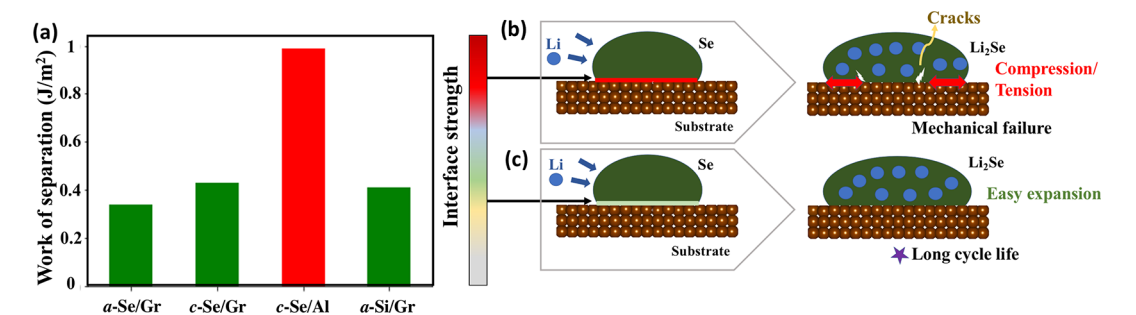


Figure 3. Interface strength quantified by work of separation (W_{sep}) results. (a) Interfacial work of separation for the relaxed a-Se/Gr, c-Se/Gr, c-Se/Al, and a-Si/Gr interfaces. (b) Schematic representation of an interface under a "high-interface-strength" condition in red, facing compressive stresses during Li incorporation in LIBs, ultimately leading to crack propagation and mechanical failures. (c) Schematic representation of a contrasting "low-interface-strength" condition as seen in the case of graphene interfaces in green/yellow. Passive interface strength permits easy expansion and contraction to the active electrode material.

Here, σ_1 and σ_2 are the surface energies of both the materials and γ_{12} is the interface energy. These are determined from the total energies of slab 1, slab 2, and slab 3 as E_1 , E_2 , and E_{12} , respectively. A is the area of contact at the interface. Besides Se/Gr, we also used similar slab models to calculate $W_{\rm sep}$ in c-Se/Al and a-Si/Gr interface systems. Details of slab energies and calculation of $W_{\rm sep}$ are presented in Section S1.

Results of W_{sep} for different interfaces are summarized in Figure 3a and indicate that interface strength for Se-Gr systems (both a- and c-Se) is comparable to that for the a-Si/ Gr interface. Lower W_{sep} was previously shown¹² to influence electrode performance positively by mitigating stresses in the Si electrode during the lithiation/delithiation cycle. Computational analyses, backed by experimental validation, suggested that a W_{sep} value of ~0.41 J m⁻² (the green interface in Figure 3c) for amorphous Si over Gr (a-Si/Gr) permits a "slippery" vdW interface where Si is loosely physisorbed on the Gr surface without any strong bonding. This allows these two materials to slip over one another in a frictionless manner without losing the mechanical contact. In contrast, the high W_{sep} (~1.6 J m⁻²) in amorphous Si over 3D Ni (a-Si/Ni) was associated with "nonslippery" high-adhesion conditions dominated by repeated compression and tension in the interfacial region (the red interface in Figure 3b). In our study, the $W_{\rm sep}$ values for a-Se/Gr and c-Se/Gr are 0.34 and 0.43 J m⁻², respectively. The comparable interface strengths of c-Se/Gr and a-Si/Gr propose a long cycle life of Se-Gr electrodes. This interface strength value between the active electrode and graphene is expected to decrease with increasing concentration of Li in the electrode based on earlier work of Stournara et al. on Si and porous C interfaces.⁵³ The validation of this trend for the Si/Gr interface can be found in Section S2. The likeliness between Si/Gr and Se/Gr interfaces suggests interface adhesion at the Se electrode and the Gr interface will decrease with the increase in Li concentration.

As alloying electrodes undergo continuous phase changes during the battery cycle, Se will have an added advantage of similar interface strength during its phase transitions (c-Se \leftrightarrow a-Se) as compared to its complementary electrodes. The $W_{\rm sep}$ of a-Se/Gr (0.34 J m $^{-2}$) is less only by 20% of c-Se/Gr (0.43 J m $^{-2}$), primarily due to the structural similarities between the two phases. a-Se derived by the quenching process was similar to c-Se in terms of first neighboring Se—Se distances (\sim 2.4 Å in Figure 1a2,b2). The only critical difference between the two allotropes of Se is that in a-Se, Se $_8$ rings break to form different-sized polymeric chains (shown in Figure 1b1). The

present structures of Se allotropes are in tune with a previous study where it is emphasized that structural parameters such as interatomic bond lengths, bond angles, and dihedral angles are comparable among Se crystalline allotropes.⁴⁶ Thus, the a-Se structure derived from the quenching of c-Se is dominated by large chain molecules having each Se atom surrounded by two immediate neighbors, with interatomic distances similar to parent c-Se. 46,57 The impact of structural variations on the interface strength of Se/Gr systems could be understood from eq 1 where W_{sep} depends on the difference between E_{12} and the sum of energies of the individual materials $(E_1 + E_2)$. The low interface energy $(\gamma_{12} = E_{12}/A)$ represents that two materials are able to come together to form a stable interface. In our calculations, the interface energy $(\gamma_{12} = E_{12}/A)$ of both the interface systems (c-Se/Gr and a-Se/Ge) is almost the same (Figure 2). However, the overall interface strength (W_{sep}) drops slightly in the a-Se/Gr system $(0.43 \rightarrow 0.34 \text{ J})$ m^{-2}) due to comparatively high surface slab energy (E_2 in Figure 2) and lower thermodynamic stability of the *a*-Se phase. The disintegrated forms of Se rings dominate the a-Se/Ge structure, resulting in high E_2 . Oppositely, the monoclinic c-Se and Gr interface system is devoid of any lattice-mismatchassociated lattice distortions. The eight-membered rings of Se are mostly conserved in the stable interface system with Gr. Upon optimization, there is only a slight vertical condensation (shown in Figure S2) of the Se crystal, resulting in minor distortions of dihedral angles and low interfacial gap (d). This works in favor of the interface in establishing a beneficial contact with Gr.

In addition to the cycle life and phase transition, lower interface strength between Se and Gr can be beneficial in designing the electrode morphology. A latest study⁴⁴ shows that high adhesion between the active electrode material (AM) and binder causes disconnected lumps of AM-binder within the electrode. Passable interface strength between the active Se electrode and Gr (as the binder) permits both the materials to be completely dispersed throughout the volume maintaining ionic and electronic conductive pathways. To present a contrast, interface strength in the c-Se/Al system was examined by evaluating W_{sep} . The replacement of 2D Gr by 3D Al affected the interface strength with a 2-fold increase (0.99 J m⁻² red interface in Figure 3). Al is also a conventional current collector used at the cathode end in LIBs. Our results suggest that by reducing the surface contact between Se and Al, the cycle life of the Se electrode can be enhanced. This contrasting adhesion of Se with Gr and Al advocates the use of Se-Gr electrodes in battery applications. The presence of Gr around active Se also defends Se from chemical decay at the electrolyte interface; however, Gr—electrolyte interface interaction has not been taken into consideration in the present analysis. Next, we investigate compelling factors that contribute to the interfacial strength in Se and Si interface systems.

Electron Exchange and Charge Separation Analysis. The low interface strength and slippery surface of Gr pose an essential question - how long does the Se-Gr interface stay intact? Se was previously reported to peel off from SiO₂/Si surfaces by slight mechanical exertion due to a lack of mechanical interlocking and chemical interaction.⁵⁸ This condition was improved by inserting an inconsistent intermediate layer of indium(In) between the Se-SiO₂ interface. A nonmetal like Se could then be held in place by forming a surface alloy of In₂Se₃. In the case of 2D materials such as Gr, even with Se-Gr interface strength being similar to the Si-Gr interface, Se-Gr might still lack stability due to polarity and the absence of dangling bonds as prevalent in the case of Si. 59,60 Applicatory longevity of Se interfaces needs to be further investigated by utilizing a comprehensive analysis of bonding. In this section, we discuss the persistence of Se-Gr interfaces as the function of electron distribution across the interface. We analyze electron exchange between the two surfaces followed by the difference in surface potential and resultant charge separation between the two materials.

Electron redistribution is a prominent reason for interface strength and can throw light on the bonding phenomenon at the interface. The overall electron exchange between 3D Se bulk and 2D Gr is studied in optimized interface supercells via Bader charge analysis using scripts by the Henkelman group. Bader charge analysis quantifies atomic charges based on the charge density in a Bader volume of each atom in the relaxed structure and calculates net charge transfer across the interface (Δq) . In light of our used pseudopotential, all the C, Si, Se, and Al atoms in the system were taken to have 4, 4, 6, and 3 valence electrons, respectively. Charge distribution on Gr was computed by summing electronic charges on all the carbon atoms in the system (q_c) . Then the total charge transfer across the interface was calculated by

$$\Delta q = q_c - 4 \times c \tag{2}$$

where c is the number of carbon atoms in the system. The resultant values are presented in Table 1 for all considered Gr interface systems. The positive value of Δq indicates the number of electrons Gr gained when in contact with the bulk material, while a negative value represents the loss in electrons.

Table 1. Summary of Electron Distributions across Gr Interfaces with Bulk Amorphous Se, Crystalline Se, and Amorphous Si along with Their Associated Interface Strength Values $(W_{\text{sep}})^a$

system	$W_{\rm sep} (\rm J m^{-2})$	$\mathrm{d}\phi/\mathrm{d}z~(\mathrm{eV}~\mathrm{\AA}^{-1})$	$\Delta q \ (e^{-1})$	d (Å)
a-Se/Gr	0.34	3.08	-0.2552	3.33
c-Se/Gr	0.43	3.03	0.3119	2.87
a-Si/Gr	0.41	2.18	0.4266	3.06

"The potential energy gradient across the interface is denoted by $\mathrm{d}\phi/\mathrm{d}z$, net charge transferred across the interface is given by Δq , where a positive value denotes the charge acquired by graphene while a negative value denotes the charge given by graphene to the bulk, and d is the distance between Gr and the lowest Se/Si atom.

The relation between the interface strength and the net charge transfer across the interface, $W_{\rm sep} \propto |\Delta q|/d^2$, for Se interfaces compares well with some previous works on Pt–Gr and Si–C interfaces. ^{53,62} In *a*-Se/Gr, *a*-Se gains net ~0.2556 electrons from Gr, leading to p-type doping in the latter. We observed that in the *a*-Se structure, Se atoms broken from the chains adsorb on the Gr surface by gaining more electrons (illustrated in Figure 4a). This result is consistent with a previous work by Nakada and Ishii, ⁶³ which highlights that while most atoms lose electrons to the Gr surface, nonmetals from Groups 16 and 17 take up electrons from Gr. Therefore, the Se atom gains about 0.01 e⁻¹ when adsorbed on the Gr surface. Our results verify that in an amorphous state, interfacial Se atoms exhibit individualism and adsorb on the Gr surface with similar characteristics.

The direction of net charge transfer is reversed in the crystalline interface system (Figure 4b), where c-Se loses electrons to Gr ($\sim 0.312 \text{ e}^{-1}$). Atoms on Se₈ in the interfacial regions have fewer electrons than the atoms in Se₈ farther from Gr. This tendency of Gr to gain electrons from interfacing 3D bulk is steady in the a-Si/Gr system where net 0.4226 e⁻¹ is gained by Gr (summarized in Table 1). These Δq values at Gr interfaces emphasize that physisorption is the primary mode of bonding at (Se/Si)-Gr interfaces. Additionally, a very distinctive interface is noted between c-Se and Al in Figure 4c, where Se₈ rings at the interface break into individual atoms to form strong covalent bonds with the Al surface. There is a surface reaction between Al and Se surface atoms resulting in $\Delta q = 4.5 \text{ e}^{-1}$ between Se and Al substrates. This reaction between Se and Al will result in the loss of active Se for reaction with the oncoming adatom in batteries (e.g., Li in lithium batteries).

Net electron exchange (Δq) at the Si–Gr interface is quantitatively more than Se–Gr interfaces (Table 1). This comparative ease of electron exchange at the Si–Gr interface can be understood with the potential gradient and charge separation analysis presented in Figure 5. To bridge the electronic character across the Se–Gr interface, we mapped the potential step (ΔV) between two materials and defined it as the potential gradient $(\mathrm{d}\phi/\mathrm{d}z)$ by dividing the difference in electrostatic potential at the interface with the interface gap (d). The computed electrostatic potential (V) on atoms was averaged in the x–y plane for every unit z dimension (normal to the Gr plane). The potentials of Se and Gr at the interface were acquired by averaging $V_{\mathrm{Se/Gr}}$ in the z dimension. The potential gradient across the interface was determined by

$$\frac{\mathrm{d}\phi}{\mathrm{d}z} = \frac{V_{\mathrm{Se}} - V_{Gr}}{d} \tag{3}$$

where $V_{\rm Se}-V_{\rm Gr}$ is the difference of V between Se and Gr atoms at the interface. The interfacial gap (d) in z dimension is the distance of the lowest Se atom from the Gr surface (see Figure 5a1-c1).

A lower potential gradient promises ease of interaction at the interface $(\mathrm{d}\phi/\mathrm{d}z \sim 0)$ for the same materials), while a large potential step is indicative of an incohesive interface with a less scope for electron exchange and bonding. The $\mathrm{d}\phi/\mathrm{d}z$ values for Se and Si interfaces with Gr are summarized in Table 1, along with their associated W_{sep} and electron exchange results. Figure 5a1,b1 demonstrates the potential step that developed across the Se–Gr interfaces and the resultant gradients. The red curve is the averaged electrostatic potential in the x-y plane, and purple is the averaged V across the z dimension.

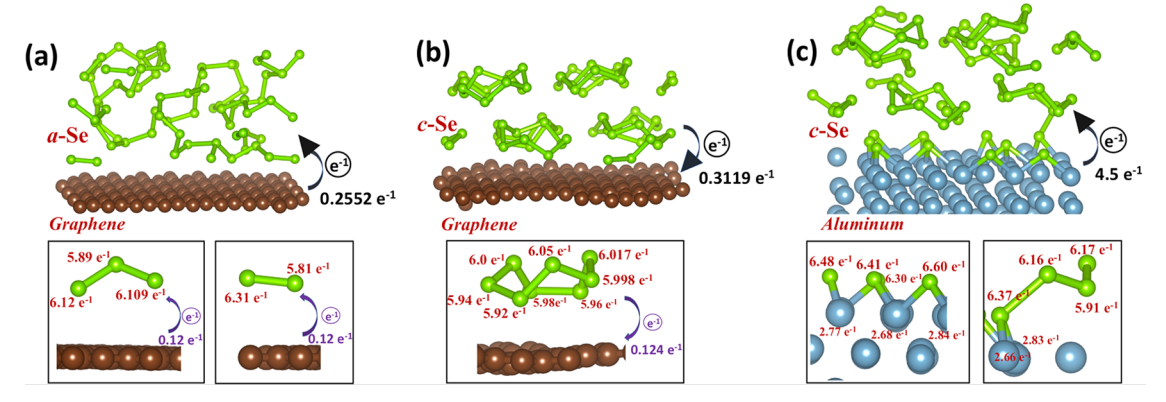


Figure 4. Distribution of electrons on Se atoms present at the graphene and aluminum interfaces. (a) Illustration of net charge transfer ($\Delta q = 0.2552 \text{ e}^{-1}$) from the Gr surface to a-Se at the a-Se/Gr interface. Se atoms detached from Se chains and attached to fewer than 2–3 Se atoms adsorb on the Gr surface by gaining more electrons ($\sim 0.12 \text{ e}^{-1}$). (b) The net charge transfer ($\Delta q = 0.3119 \text{ e}^{-1}$) at the c-Se/Gr interface is directed toward Gr. Se atoms within Se₈ rings in the interfacial region have a lower number of electrons than Se atoms farther from the Gr surface. (c) Optimized view of the c-Se/Al interface where Se₈ rings at the interface break into individual atoms to form covalent bonds with surface Al atoms. This surface reaction between Al and Se results in comparatively high net charge transfer ($\Delta q = 4.5 \text{ e}^{-1}$) between Se and Al substrate. All atomic charges were obtained via Bader charge analysis.

The difference in average potentials of a-Se and Gr in the interface system is the highest (Figure 5a1). This results in a sizeable potential step and a steep value of $d\phi/dz$ (3.081 eV $Å^{-1}$). A similar trend is noted in the case of the c-Se/Gr interface in Figure 5b1, where the $d\phi/dz$ value is 3.03 eV Å⁻¹ and d = 2.86 Å. This curtailed value of $d\phi/dz$ and d indicate that the c-Se/Gr interface system might be slightly superior to its amorphous counterpart in terms of bonding ability. In comparison to Se-Gr interfaces, a-Si/Gr has a reduced potential step across the interface and the resulting $d\phi/dz$ (2.18 eV Å^{-1}) is significantly lower (Figure 5c1). Hence, we observe higher electron exchange at the a-Si/Gr interface than c-Se/Gr despite having comparative $W_{\rm sep}$ values. The ${
m d}\phi/{
m d}z$ values indicate that Se is less likely to remain bonded with Gr as compared to the case of Si/Gr. The absence of interfacial bonds at Gr interfaces is further evident with distant potential wells near the interface. This observation is in contrast to the *c*-Se/Al interface where the presence of an additional potential well is noted due to surface chemical reaction between Se and Al (see Figure S3).

Charge density in the interfacial region was visualized by charge separation analysis. The charge separation scheme at the interface was extracted by subtracting the charge densities of individual materials from that of the entire system, and the difference is plotted with an isosurface of 0.00024 e Å⁻³. The resultant plots in Figure 5a2-c2 provide the extent of interaction between the atomic systems and are consistent with our Δq and $\mathrm{d}\phi/\mathrm{d}z$ results. The charge separation scheme for Se interfaces exhibits hardly any overlap of electron clouds between the two materials. Nevertheless, there is a presence of a strong dipole at the interface due to accumulation of negative and positive charges, as indicated by the red and green isosurfaces. Charge separation of c-Se/Gr (Figure 5b2) suggests that the crystalline phase of Se is better than a-Se in forming a reliable interface with Gr as indicated by some overlap of positive and negative isosurfaces at the interface. The charge separation scheme of the a-Si/Gr interface exhibits a better overlap of electron clouds between the two materials. These findings further imply that Se-Gr interfaces are not as amicable as Si-Gr, and Se alone can easily disintegrate from the Gr surface upon external stimulation.

Electronic Conductivity in the Se-Gr Interface Systems. In order to understand the differences in electronic conductivity of Se allotropes when interfaced with Gr, we have incorporated DOS analysis for a-Se, c-Se, and their respective Gr interface systems. DOS analysis gives an idea about the number of states that electrons are allowed to occupy at a particular energy level in a system. In principle, the distribution of electronic states near the Fermi level (denoted by the dark dashed line in Figure 6) is noted. Since our work focuses on how the Gr interface changes for two different Se allotropes, we first analyzed DOS plots of a-Se and c-Se without a Gr substrate in Figure 6a,b. We find that the overall appearance of DOS changed between a-Se and c-Se. In particular, there is a significant reduction in the band gap in the total DOS plot of a-Se in comparison to c-Se. The band gap between the valence band (VB) and conduction band (CB) in c-Se is 1.6 eV (Figure 6b), which is reduced to 0.16 eV in a-Se (Figure 6a). Moreover, energy states that are discrete for c-Se become more continuous in a-Se as existent peaks broaden and new energy levels are introduced due to the formation of disintegrated Se chains of different lengths. Even when the amorphous phase of Se looks more promising in terms of electronic conductivity by reduction of the band gap, the electron mobility is compromised in these extended states.⁶⁶ Thus, the band gap in c-Se is replaced with the mobility gap in a-Se.

Next, we plotted total DOS for Se and Gr when interfaced in a-Se/Gr and c-Se/Gr systems (see Figure 6c,d) to interpret the influence of the Gr substrate on the electronic properties of Se and vice versa. In the c-Se/Gr system, the presence of Gr with c-Se works to slightly improve the conductivity in Se. First, the band gap in total DOS of Se (green) was 1.6 eV before being reduced to 1 eV. The distinct peaks of c-Se become broader in c-Se/Gr to show explicit continuity of energy states in the VB and CB (Figure 6d). Next, a red shift (toward lower energy) of all labeled peaks of c-Se is seen due to the presence of Gr. This shift of peaks is on account of changes observed in dihedral angles of the relaxed c-Se structure over the Gr surface. In addition, some additional peaks are introduced due to the overlap of selenium's 3d orbitals and carbon's p orbitals. The effects of the Gr substrate on the electronic properties of Se are slightly reversed in the case of a-Se/Gr. In contrast to its crystalline allotrope, the presence of Gr brought about

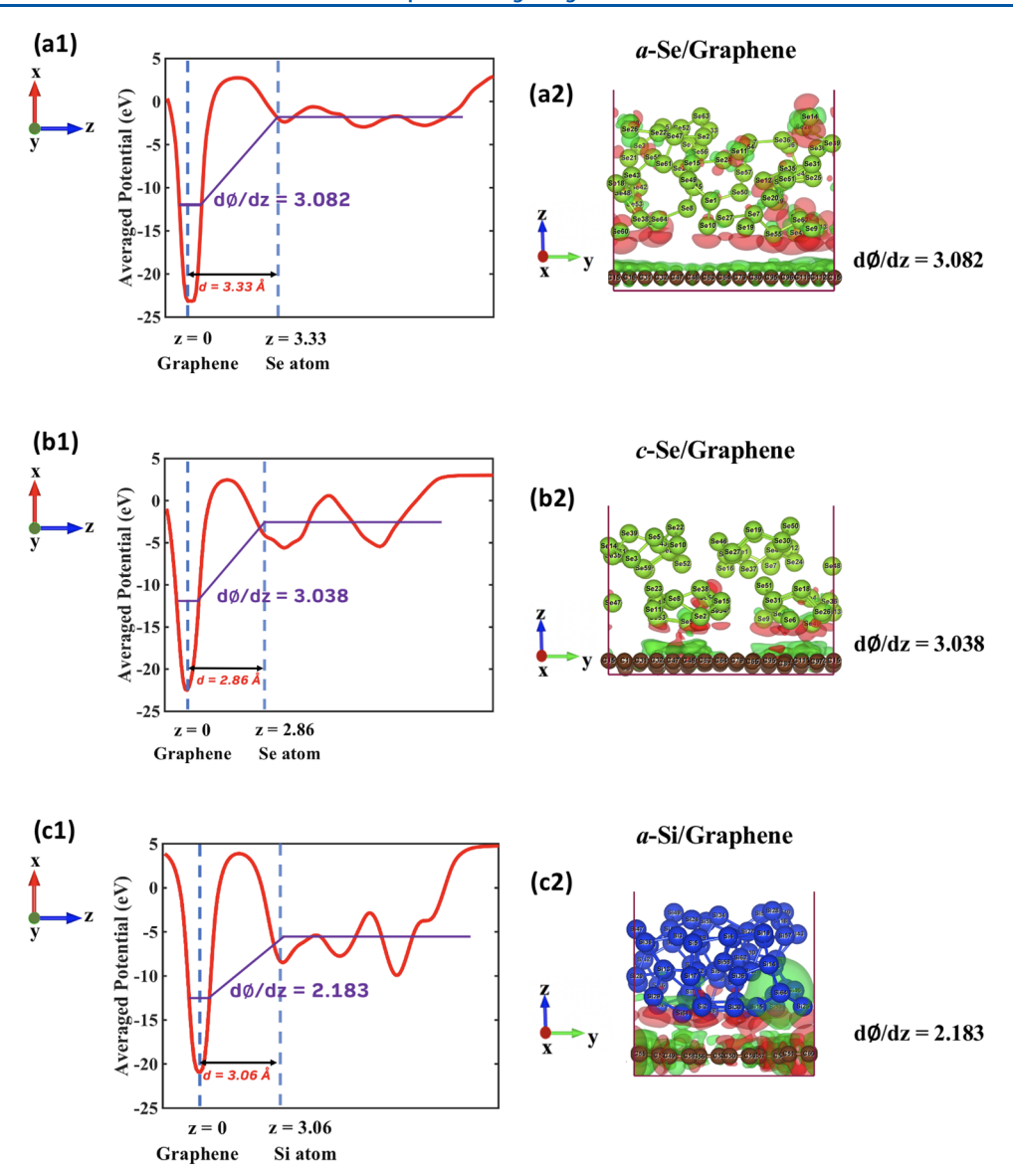


Figure 5. Comparison of the potential gradient and charge separation at graphene interfaces. (a1-c1) Planar average potential curves at graphene interfaces with amorphous Se, crystalline Se, and amorphous Si. The red curve is the averaged electrostatic potential in the x-y plane, and purple is the averaged potential across the z dimension. There is a potential step across all the interfaces that results in potential gradients ($d\phi/dz$). d denotes the distance of the nearest Se/Si atom with respect to the Gr sheet. (a2-c2) Charge separation schemes for Gr interfaces with amorphous Se, crystalline Se, and amorphous Si. Charge accumulation and depletion are shown in red and green, respectively. In comparison to Se-Gr interfaces, a-Si/Gr has a reduced potential step ($d\phi/dz = 2.18 \text{ eV Å}^{-1}$) and significant overlap of electron clouds across the interface representing the ease of interfacial interaction. A large potential gradient ($d\phi/dz$) at Se-Gr interfaces is indicative of an incohesive interface with a less scope for electron exchange and bonding.

redistribution of states near the band gap. A recession of the CB and VB is noted, which has introduced a wider band gap in the total DOS of *a*-Se in Figure 6c in comparison to Figure 6a. The energy between the CB of *a*-Se, occupied by 3d electrons, and VB dominated by p orbital electrons increases from 0.16 to 0.4 eV due to interference of Gr orbitals with Se. The localization of states near the band gap works in favor of reducing the mobility gap in *a*-Se. The mobilities in these defined localized states can thus be controlled with thermally activated tunneling. Overall, the continuity of electronic states in total DOS of *a*-Se/Gr indicates enhanced conductivity.

The presence of surface Se also impacts the electronic properties of Gr as demonstrated in the total DOS plots of pristine and Se-doped Gr in Figure 7. Gr is a semimetal known for its characteristic cone that conjoins the VB and CB at the

minimum conductivity point also known as the Dirac point at 0 eV. 67 Due to the presence of c-Se, the total DOS curve of Gr in c-Se/Gr deviates from its signature cone structure with incorporation of some additional states near 0 eV as it gains electrons. A very small band gap of 0.10 eV is introduced near 0 eV in the electronic states of Gr interfaced with monoclinic Se (see Figure 7c). The surface charge states of Gr due to π electrons are known to be sensitive to surface charge distribution. We suggest that spread of Se $_8$ rings of monoclinic Se on the surface of Gr causes inconsistent charge densities on the Gr surface (can also be seen in Figure 5b2). This redistribution of surface charges is the potential reason for the opening of the band gap in Gr. This band gap is desirable for device applications in order to control the behavior of charge carriers and hence can be effectively engineered based on the

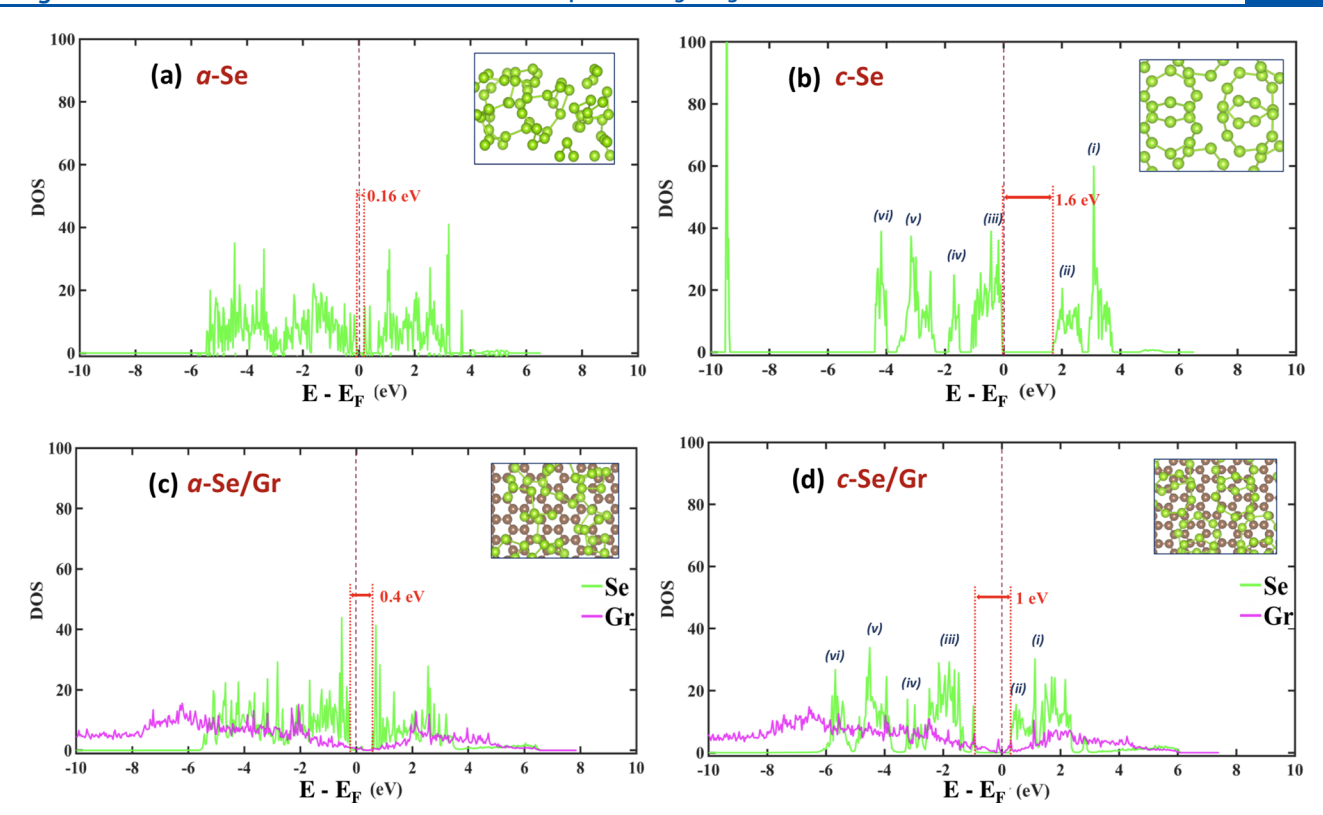


Figure 6. Total density of states (DOS) plots of Se allotropes and Se interfaced with graphene. The green and pink plot indicate the total DOS of Se and Gr in the system, respectively. (a) DOS of isolated amorphous selenium (a-Se). Energy states are continuous with a very small band gap of 0.16 eV. (b) DOS of isolated monoclinic selenium (c-Se). Energy states are discrete, and peaks are labeled as (i-vi). There is a difference of 1.6 eV between the valence band (VB) and conduction band (CB). (c) t-DOS of amorphous selenium over the graphene substrate (a-Se/Gr). The difference between the VB and CB in a-Se increases to 0.4 eV. (d) t-DOS of monoclinic selenium over the graphene substrate (c-Se/Gr). All the labeled peaks shift toward lower energy as the energy difference between the VB and CB is reduced to 1 eV.

characteristics of the chemical dopant (active c-Se in this case). In contrast, graphene DOS maintains its distinctive conical structure in a-Se/Gr as shown in Figure 7b. Through the loss of electrons to Se, the minimum conductivity point in Gr shifts toward a positive gate voltage of 0.4 eV from 0 eV. This shift is similar to the DOS of p-type doped Gr in a previous study.⁶⁸ Due to structural inconsistencies in the amorphous state of Se, the count of dopant acceptor Se atoms can vary, which will influence the mobility of charge carriers in Gr. Free acceptor Se atoms at the a-Se/Gr interface function to modulate electron concentrations. Overall, the total DOS plot of Gr in c-Se/Gr and a-Se/Gr resonates well with our Bader charge analysis (Δq) and charge separation results. This differential doping of Gr due to Se contact could result in two regimes of Gr in the system as n-doped and p-doped Gr. These regimes are not expected to be homogeneous and hence could result in modulated electrical contact at Gr edges.⁶⁹

CONCLUSIONS

In conclusion, we performed a comparative study of interfacial characteristics for the Se–Gr interface and distinguished Si–Gr interface. By first-principles calculations, we probed the Gr interface with two different Se allotropes, namely, monoclinic and amorphous, for strength, long-term stability, and electronic conductivity. Our work of separation results show that Se–Gr interfaces have interface strengths (0.43 and 0.34 J m⁻²) comparable to the amorphous Si–Gr interface (0.41 J m⁻²), and therefore, Se/Gr interface systems promise to retain the benefits of the Si–Gr interface in terms of mitigating interfacial

stresses during ion battery cycles. There is only a small variation in interface strength when Se change phase from monoclinic to amorphous. The structural analysis of the interfaces reveals the cause of this minimal variation in interface strength to be similarities in Se-Se bond lengths and polymeric chains among Se allotropes. This gives the Se/Gr electrode an advantage over its contemporaries as it could be assured that interface strength will not undergo extreme transitions during phase changes. However, Se-Gr interfaces can unbind quite easily due to polarity (potential gradient $\mathrm{d}\phi/$ $dz = 3.03 \text{ eV Å}^{-1}$) and the lack of stable chemical interaction (net electron exchange $\Delta q = 0.3119 \text{ e}^{-1}$) between both the materials if electrode morphologies are not carefully designed. In contrast to the effects noted on interface strength, the phase transition of Se can modify the electronic characteristics of the Se-Gr interface. The Bader charge analysis along with the DOS plots of the Gr interface with amorphous and crystalline Se denotes p- and n-type doping of Gr, respectively. Our analysis suggests that crystalline Se forms an enhanced interface with Gr in terms of strength and electronic conductivity compared to its amorphous Se counterpart.

As our computational results provide a deeper insight into the interface between two different allotropes of selenium with pristine graphene, the variations in the structure of selenium are the focal point of the presented interface analysis. There is a further scope for the analysis to be extended for variations in graphene morphologies such as wrinkles, point defects, doping, and multiple layers. Earlier works on adsorption potential of doped 70,71 and defected graphene 1,72 suggest a possible

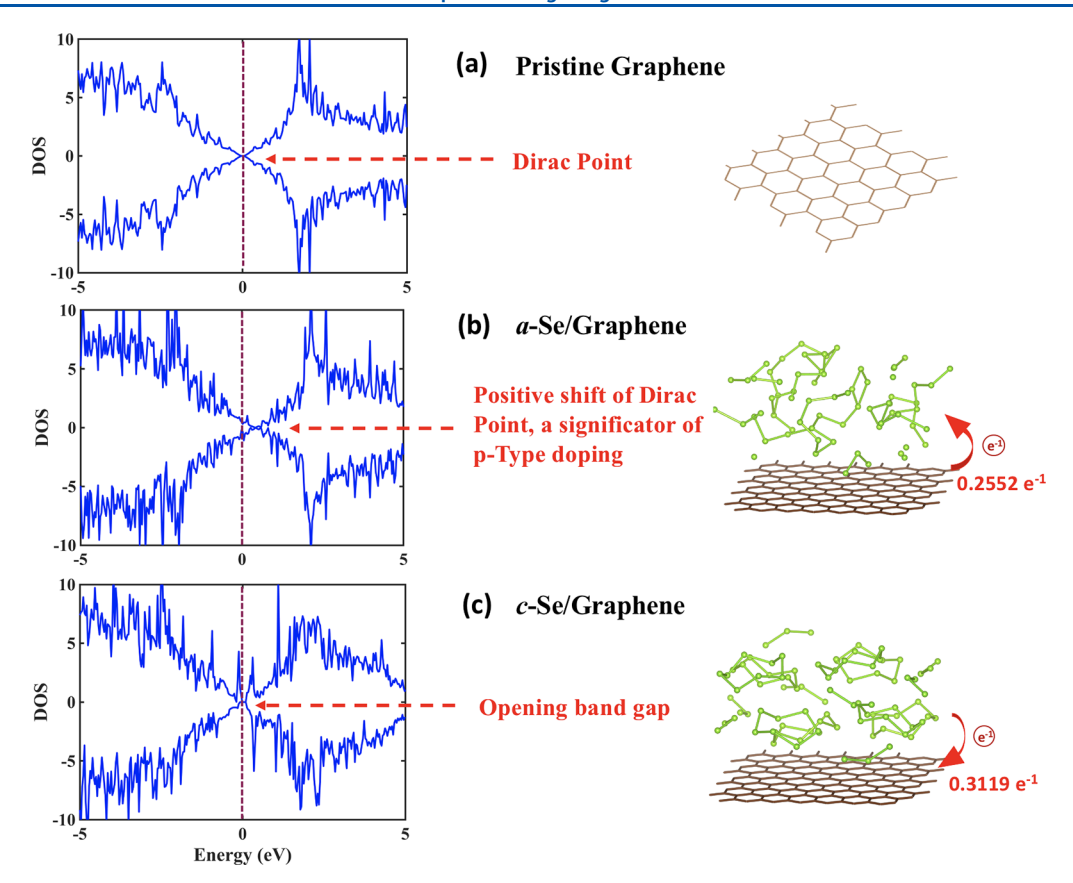


Figure 7. Changes in total DOS of graphene. (a) DOS of pristine graphene having the Dirac point at 0 eV where the VB and CB meet. (b) Total DOS of graphene when interfaced with amorphous Se (a-Se). Due to surface charge doping of graphene by a-Se, the Dirac point shifts toward 0.4 eV. (c) Total DOS of graphene when interfaced with monoclinic Se (c-Se) deviates from its signature cone structure with incorporation of some additional states near 0 eV as it gains electrons and introduction of a very small band gap of 0.10 eV near 0 eV.

increase of the interface strength between 3D Se bulk and defected 2D graphene, which has further widened the scope of the Se–Gr interface in technologies such as solar cells.⁴⁵

ASSOCIATED CONTENT

Supporting Information

The Supporting Information is available free of charge at https://pubs.acs.org/doi/10.1021/acs.langmuir.0c02893.

Energies of surface slabs for Se interface systems; variation in graphene interface strength as Li concentration varies; distortions in the Se crystal in the c-Se/Gr interface; planar averaged potential in the c-Se/Al interface system; surface energies of selenium structures (PDF)

AUTHOR INFORMATION

Corresponding Authors

David Mitlin — Materials Science and Engineering Program & Texas Materials Institute, The University of Texas at Austin, Austin, Texas 78712-1591, United States; oocid.org/0000-0002-7556-3575; Email: david.mitlin@austin.utexas.edu

Dibakar Datta — Department of Mechanical and Industrial Engineering, New Jersey Institute of Technology, Newark, New Jersey 07103, United States; ⊚ orcid.org/0000-0003-0233-3581; Email: dibakar.datta@njit.edu

Author

Vidushi Sharma — Department of Mechanical and Industrial Engineering, New Jersey Institute of Technology, Newark, New Jersey 07103, United States; orcid.org/0000-0002-4576-4990

Complete contact information is available at: https://pubs.acs.org/10.1021/acs.langmuir.0c02893

Author Contributions

All authors have given approval to the final version of the manuscript.

Notes

I

The authors declare no competing financial interest.

The data reported in this paper is available from the corresponding author upon reasonable request.

The pre- and postprocessing codes used in this paper are available from the corresponding author upon reasonable request. Restrictions apply to the availability of the simulation codes, which were used under license for this study.

ACKNOWLEDGMENTS

D.M. (co-conception and guidance of research, preparation of the manuscript) was supported by the National Science Foundation, Civil, Mechanical and Manufacturing Innovation (CMMI), Award Number 1911905. V.S. (computation, manuscript preparation) and D.D. (co-conception and guidance of research, preparation of the manuscript) were supported by NSF (Award Number 1911900). D.D. acknowl-

edges the Extreme Science and Engineering Discovery Environment (XSEDE) for the computational facilities (Award Number – DMR180013). V.S. acknowledges Dr. Kamalika Ghatak for the fruitful discussion during the project.

REFERENCES

- (1) Datta, D.; Li, J.; Koratkar, N.; Shenoy, V. B. Enhanced lithiation in defective graphene. *Carbon* **2014**, *80*, 305–310.
- (2) Buldum, A.; Tetiker, G. First-principles study of graphenelithium structures for battery applications. *J. Appl. Phys.* **2013**, *113*, 154312.
- (3) Chou, S.-L.; Wang, J.-Z.; Choucair, M.; Liu, H.-K.; Stride, J. A.; Dou, S.-X. Enhanced reversible lithium storage in a nanosize silicon/graphene composite. *Electrochem. Commun.* **2010**, *12*, 303–306.
- (4) Luo, J.; Zhao, X.; Wu, J.; Jang, H. D.; Kung, H. H.; Huang, J. Crumpled graphene-encapsulated Si nanoparticles for lithium ion battery anodes. *J. Phys. Chem. Lett.* **2012**, *3*, 1824–1829.
- (5) Wen, Y.; Zhu, Y.; Langrock, A.; Manivannan, A.; Ehrman, S. H.; Wang, C. Graphene-bonded and -encapsulated Si nanoparticles for lithium ion battery anodes. *Small* **2013**, *9*, 2810–2816.
- (6) Ji, J.; Ji, H.; Zhang, L. L.; Zhao, X.; Bai, X.; Fan, X.; Zhang, F.; Ruoff, R. S. Graphene-encapsulated Si on ultrathin-graphite foam as anode for high capacity lithium-ion batteries. *Adv. Mater.* **2013**, 25, 4673–4677.
- (7) Ko, M.; Chae, S.; Jeong, S.; Oh, P.; Cho, J. Elastic a-silicon nanoparticle backboned graphene hybrid as a self-compacting anode for high-rate lithium ion batteries. *ACS Nano* **2014**, *8*, 8591–8599.
- (8) Zhao, M.-Q.; Zhang, Q.; Huang, J.-Q.; Tian, G.-L.; Nie, J.-Q.; Peng, H.-J.; Wei, F. Unstacked double-layer templated graphene for high-rate lithium—sulphur batteries. *Nat. Commun.* **2014**, *5*, 3410.
- (9) Zhou, G.; Pei, S.; Li, L.; Wang, D. W.; Wang, S.; Huang, K.; Yin, L. C.; Li, F.; Cheng, H. M. A graphene-pure-sulfur sandwich structure for ultrafast, long-life lithium-sulfur batteries. *Adv. Mater.* **2014**, *26*, *625*–*631*.
- (10) Datta, M. K.; Epur, R.; Saha, P.; Kadakia, K.; Park, S. K.; Kumta, P. N. Tin and graphite based nanocomposites: Potential anode for sodium ion batteries. *J. Power Sources* **2013**, 225, 316–322.
- (11) Yang, Y.; Zheng, G.; Cui, Y. Nanostructured sulfur cathodes. Chem. Soc. Rev. 2013, 42, 3018–3032.
- (12) Basu, S.; Suresh, S.; Ghatak, K.; Bartolucci, S. F.; Gupta, T.; Hundekar, P.; Kumar, R.; Lu, T.-M.; Datta, D.; Shi, Y.; Koratkar, N. Utilizing van der Waals slippery interfaces to enhance the electrochemical stability of Silicon film anodes in Lithium-ion batteries. ACS Appl. Mater. Interfaces 2018, 10, 13442–13451.
- (13) Rana, K.; Singh, J.; Lee, J.-T.; Park, J. H.; Ahn, J.-H. Highly conductive freestanding graphene films as anode current collectors for flexible lithium-ion batteries. ACS Appl. Mater. Interfaces 2014, 6, 11158–11166.
- (14) Park, M.-S.; Rajendran, S.; Kang, Y.-M.; Han, K.-S.; Han, Y.-S.; Lee, J.-Y. Si–Ni alloy—graphite composite synthesized by arc-melting and high-energy mechanical milling for use as an anode in lithium-ion batteries. *J. Power Sources* **2006**, *158*, 650–653.
- (15) Schmuelling, G.; Winter, M.; Placke, T. Investigating the Mg—Si binary system via combinatorial sputter deposition as high energy density anodes for lithium-ion batteries. *ACS Appl. Mater. Interfaces* **2015**, *7*, 20124–20133.
- (16) Datta, M. K.; Kumta, P. N. Silicon and carbon based composite anodes for lithium ion batteries. *J. Power Sources* **2006**, *158*, 557–563.
- (17) Shu, J.; Li, H.; Yang, R.; Shi, Y.; Huang, X. Cage-like carbon nanotubes/Si composite as anode material for lithium ion batteries. *Electrochem. Commun.* **2006**, *8*, 51–54.
- (18) Lv, D.; Zheng, J.; Li, Q.; Xie, X.; Ferrara, S.; Nie, Z.; Mehdi, L. B.; Browning, N. D.; Zhang, J.-G.; Graff, G. L.; Liu, J.; Xiao, J. High energy density lithium—sulfur batteries: challenges of thick sulfur cathodes. *Adv. Energy Mater.* **2015**, *5*, 1402290.
- (19) Mikhaylik, Y. V.; Akridge, J. R. Polysulfide shuttle study in the Li/S battery system. J. Electrochem. Soc. 2004, 151, A1969.

- (20) Pang, Q.; Liang, X.; Kwok, C. Y.; Nazar, L. F. Advances in lithium—sulfur batteries based on multifunctional cathodes and electrolytes. *Nat. Energy* **2016**, *1*, 16132.
- (21) Xu, G.; Ding, B.; Pan, J.; Nie, P.; Shen, L.; Zhang, X. High performance lithium—sulfur batteries: advances and challenges. *J. Mater. Chem. A* **2014**, *2*, 12662–12676.
- (22) Su, D.; Zhou, D.; Wang, C.; Wang, G. Lithium-Sulfur Batteries: Toward High Performance Lithium—Sulfur Batteries Based on Li₂S Cathodes and Beyond: Status, Challenges, and Perspectives (Adv. Funct. Mater. 38/2018). Adv. Funct. Mater. 2018, 28, 1870273.
- (23) Zhang, J.; Yin, Y.-X.; You, Y.; Yan, Y.; Guo, Y.-G. A High-Capacity Tellurium@ Carbon Anode Material for Lithium-Ion Batteries. *Energy Technol.* **2014**, *2*, 757–762.
- (24) Liu, Y.; Wang, J.; Xu, Y.; Zhu, Y.; Bigio, D.; Wang, C. Lithium—tellurium batteries based on tellurium/porous carbon composite. *J. Mater. Chem. A* **2014**, *2*, 12201–12207.
- (25) Seo, J.-U.; Seong, G.-K.; Park, C.-M. Te/C nanocomposites for Li-Te secondary batteries. *Sci. Rep.* **2015**, *5*, 7969.
- (26) Ding, N.; Chen, S.-F.; Geng, D.-S.; Chien, S.-W.; An, T.; Hor, T. S. A.; Liu, Z.-L.; Yu, S.-H.; Zong, Y. Tellurium@ Ordered Macroporous Carbon Composite and Free-Standing Tellurium Nanowire Mat as Cathode Materials for Rechargeable Lithium—Tellurium Batteries. Adv. Energy Mater. 2015, 5, 1401999.
- (27) Abouimrane, A.; Dambournet, D.; Chapman, K. W.; Chupas, P. J.; Weng, W.; Amine, K. A new class of lithium and sodium rechargeable batteries based on selenium and selenium—sulfur as a positive electrode. *J. Am. Chem. Soc.* **2012**, *134*, 4505–4508.
- (28) Liu, L.; Hou, Y.; Wu, X.; Xiao, S.; Chang, Z.; Yang, Y.; Wu, Y. Nanoporous selenium as a cathode material for rechargeable lithium—selenium batteries. *Chem. Commun.* **2013**, *49*, 11515–11517.
- (29) Lee, J. T.; Kim, H.; Oschatz, M.; Lee, D.-C.; Wu, F.; Lin, H.-T.; Zdyrko, B.; Cho, W. I.; Kaskel, S.; Yushin, G. Micro- and Mesoporous Carbide-Derived Carbon—Selenium Cathodes for High-Performance Lithium Selenium Batteries. *Adv. Energy Mater.* **2015**, *5*, 1400981.
- (30) Cui, Y.; Abouimrane, A.; Lu, J.; Bolin, T.; Ren, Y.; Weng, W.; Sun, C.; Maroni, V. A.; Heald, S. M.; Amine, K. (De)Lithiation mechanism of Li/SeS_x (x= 0–7) batteries determined by in situ synchrotron X-ray diffraction and X-ray absorption spectroscopy. *J. Am. Chem. Soc.* **2013**, *135*, 8047–8056.
- (31) Yang, C.-P.; Xin, S.; Yin, Y.-X.; Ye, H.; Zhang, J.; Guo, Y.-G. An advanced selenium—carbon cathode for rechargeable lithium—selenium batteries. *Angew. Chem., Int. Ed.* **2013**, *52*, 8363—8367.
- (32) Li, Q.; Liu, H.; Yao, Z.; Cheng, J.; Li, T.; Li, Y.; Wolverton, C.; Wu, J.; Dravid, V. P. Electrochemistry of selenium with sodium and lithium: kinetics and reaction mechanism. *ACS Nano* **2016**, *10*, 8788–8795.
- (33) Zhang, Z.; Yang, X.; Guo, Z.; Qu, Y.; Li, J.; Lai, Y. Selenium/carbon-rich core—shell composites as cathode materials for rechargeable lithium—selenium batteries. *J. Power Sources* **2015**, 279, 88—93.
- (34) Xue, P.; Zhai, Y.; Wang, N.; Zhang, Y.; Lu, Z.; Liu, Y.; Bai, Z.; Han, B.; Zou, G.; Dou, S. Selenium@ Hollow mesoporous carbon composites for high-rate and long-cycling lithium/sodium-ion batteries. *Chem. Eng. J.* **2020**, 123676.
- (35) Zhou, J.; Chen, M.; Wang, T.; Li, S.; Zhang, Q.; Zhang, M.; Xu, H.; Liu, J.; Liang, J.; Zhu, J.; Duan, X. Covalent Selenium Embedded in Hierarchical Carbon Nanofibers for Ultra-High Areal Capacity Li-Se Batteries. *Iscience* **2020**, 23, 100919.
- (36) Li, Z.; Yuan, L.; Yi, Z.; Liu, Y.; Huang, Y. Confined selenium within porous carbon nanospheres as cathode for advanced Li–Se batteries. *Nano Energy* **2014**, *9*, 229–236.
- (37) Xi, K.; Kidambi, P. R.; Chen, R.; Gao, C.; Peng, X.; Ducati, C.; Hofmann, S.; Kumar, R. V. Binder free three-dimensional sulphur/few-layer graphene foam cathode with enhanced high-rate capability for rechargeable lithium sulphur batteries. *Nanoscale* **2014**, *6*, 5746–5753.
- (38) Zhang, J.; Xu, Y.; Fan, L.; Zhu, Y.; Liang, J.; Qian, Y. Graphene—encapsulated selenium/polyaniline core—shell nanowires

- with enhanced electrochemical performance for Li-Se batteries. *Nano Energy* **2015**, *13*, 592–600.
- (39) Kundu, D.; Krumeich, F.; Nesper, R. Investigation of nanofibrous selenium and its polypyrrole and graphene composite as cathode material for rechargeable Li-batteries. *J. Power Sources* **2013**, 236. 112–117.
- (40) Han, K.; Liu, Z.; Shen, J.; Lin, Y.; Dai, F.; Ye, H. A Free-Standing and Ultralong-Life Lithium-Selenium Battery Cathode Enabled by 3D Mesoporous Carbon/Graphene Hierarchical Architecture. *Adv. Funct. Mater.* **2015**, 25, 455–463.
- (41) Fan, X.-Y.; Ke, F.-S.; Wei, G.-Z.; Huang, L.; Sun, S.-G. Sn-Co alloy anode using porous Cu as current collector for lithium ion battery. *J. Alloys Compd.* **2009**, *476*, 70–73.
- (42) Kang, S.; Xie, H.; Zhai, W.; Ma, Z.-f.; Wang, R.; Zhang, W. Enhancing performance of a lithium ion battery by optimizing the surface properties of the current collector. *Int. J. Electrochem. Sci.* **2015**, *10*, 2324–2335.
- (43) Jeon, H.; Cho, I.; Jo, H.; Kim, K.; Ryou, M.-H.; Lee, Y. M. Highly rough copper current collector: improving adhesion property between a silicon electrode and current collector for flexible lithiumion batteries. *RSC Adv.* **2017**, *7*, 35681–35686.
- (44) Srivastava, I.; Bolintineanu, D. S.; Lechman, J. B.; Roberts, S. A. Controlling Binder Adhesion to Impact Electrode Mesostructures and Transport. ACS Appl. Mater. Interfaces 2020, 12, 34919–34930.
- (45) Meng, X.; Yu, C.; Song, X.; Iocozzia, J.; Hong, J.; Rager, M.; Jin, H.; Wang, S.; Huang, L.; Qiu, J.; Lin, Z. Scrutinizing defects and defect density of selenium-doped graphene for high-efficiency triiodide reduction in dye-sensitized solar cells. *Angew. Chem.* **2018**, 57, 4682–4686.
- (46) Goldan, A. H.; Li, C.; Pennycook, S. J.; Schneider, J.; Blom, A.; Zhao, W. Molecular structure of vapor-deposited amorphous selenium. *J. Appl. Phys.* **2016**, *120*, 135101.
- (47) Johari, P.; Qi, Y.; Shenoy, V. B. The mixing mechanism during lithiation of Si negative electrode in Li-ion batteries: an ab initio molecular dynamics study. *Nano Lett.* **2011**, *11*, 5494–5500.
- (48) Sharma, V.; Ghatak, K.; Datta, D. Amorphous germanium as a promising anode material for sodium ion batteries: a first principle study. *J. Mater. Sci.* **2018**, *53*, 14423–14434.
- (49) Kresse, G.; Furthmüller, J. Efficient iterative schemes for ab initio total-energy calculations using a plane-wave basis set. *Phys. Rev.* B **1996**, 54, 11169.
- (50) Kresse, G.; Joubert, D. From ultrasoft pseudopotentials to the projector augmented-wave method. *Phys. Rev. B* **1999**, *59*, 1758.
- (51) Blöchl, P. E. Projector augmented-wave method. Phys. Rev. B 1994, 50, 17953.
- (52) Perdew, J. P.; Burke, K.; Ernzerhof, M. Generalized gradient approximation made simple. *Phys. Rev. Lett.* **1996**, *77*, 3865.
- (53) Stournara, M. E.; Qi, Y.; Shenoy, V. B. From ab initio calculations to multiscale design of Si/C core—shell particles for Liion anodes. *Nano Lett.* **2014**, *14*, 2140–2149.
- (54) Dion, M.; Rydberg, H.; Schröder, E.; Langreth, D. C.; Lundqvist, B. I. Van der Waals density functional for general geometries. *Phys. Rev. Lett.* **2004**, *92*, 246401.
- (55) Klimeš, J.; Bowler, D. R.; Michaelides, A. Chemical accuracy for the van der Waals density functional. *J. Phys.: Condens. Matter* **2010**, 22, No. 022201.
- (56) Klimeš, J.; Bowler, D. R.; Michaelides, A. Van der Waals density functionals applied to solids. *Phys. Rev. B* **2011**, *83*, 195131.
- (57) Escoffery, C. A.; Halperin, S. Studies on the Polymorphic Transformation of Selenium. *Trans. Electrochem. Soc.* **1946**, *90*, 163.
- (58) Chen, Y.-Z.; You, Y.-T.; Chen, P.-J.; Li, D.; Su, T.-Y.; Lee, L.; Shih, Y.-C.; Chen, C.-W.; Chang, C.-C.; Wang, Y.-C.; Hong, C.-Y.; Wei, T.-C.; Ho, J. C.; Wei, K.-H.; Shen, C.-H.; Chueh, Y.-L. Environmentally and mechanically stable selenium 1D/2D hybrid structures for broad-range photoresponse from ultraviolet to infrared wavelengths. ACS Appl. Mater. Interfaces 2018, 10, 35477–35486.
- (59) Tao, M.; Udeshi, D.; Basit, N.; Maldonado, E.; Kirk, W. P. Removal of dangling bonds and surface states on silicon (001) with a monolayer of selenium. *Appl. Phys. Lett.* **2003**, *82*, 1559–1561.

- (60) Lannoo, M. The role of dangling bonds in the properties of surfaces and interfaces of semiconductors. *Rev. Phys. Appl.* **1990**, 25, 887–894.
- (61) Sanville, E.; Kenny, S. D.; Smith, R.; Henkelman, G. Improved grid-based algorithm for Bader charge allocation. *J. Comput. Chem.* **2007**, 28, 899–908.
- (62) Sen, F. G.; Qi, Y.; Alpas, A. T. Anchoring platinum on graphene using metallic adatoms: a first principles investigation. *J. Phys.: Condens. Matter* **2012**, 24, 225003.
- (63) Nakada, K.; Ishii, A. Migration of adatom adsorption on graphene using DFT calculation. *Solid State Commun.* **2011**, *151*, 13–16.
- (64) Peressi, M.; Binggeli, N.; Baldereschi, A. Band engineering at interfaces: theory and numerical experiments. *J. Phys. D: Appl. Phys.* 1998, 31, 1273.
- (65) Li, D. Y.; Guo, L.; Li, L.; Lu, H. Electron work function—a probe for interfacial diagnosis. *Sci. Rep.* **2017**, *7*, 9673.
- (66) Mott, N. F.; Davis, E. A.; Street, R. A. States in the gap and recombination in amorphous semiconductors. *Philos. Mag.* **1975**, *32*, 961–996.
- (67) Novoselov, K. S.; Morozov, S. V.; Mohinddin, T. M. G.; Ponomarenko, L. A.; Elias, D. C.; Yang, R.; Barbolina, I. I.; Blake, P.; Booth, T. J.; Jiang, D.; Giesbers, J.; Hill, E. W.; Geim, A. K. Electronic properties of graphene. *Phys. Status Solidi B* **2007**, 244, 4106–4111.
- (68) Tang, Y.-B.; Yin, L.-C.; Yang, Y.; Bo, X.-H.; Cao, Y.-L.; Wang, H.-E.; Zhang, W.-J.; Bello, I.; Lee, S.-T.; Cheng, H.-M.; Lee, C.-S. Tunable band gaps and p-type transport properties of boron-doped graphenes by controllable ion doping using reactive microwave plasma. *ACS Nano* **2012**, *6*, 1970–1978.
- (69) Lee, E. J. H.; Balasubramanian, K.; Weitz, R. T.; Burghard, M.; Kern, K. Contact and edge effects in graphene devices. *Nat. Nanotechnol.* **2008**, *3*, 486–490.
- (70) Zhou, Y. G.; Zu, X. T.; Gao, F.; Nie, J. L.; Xiao, H. Y. Adsorption of hydrogen on boron-doped graphene: A first-principles prediction. *J. Appl. Phys.* **2009**, *105*, No. 014309.
- (71) Dai, J.; Yuan, J. Adsorption of molecular oxygen on doped graphene: Atomic, electronic, and magnetic properties. *Phys. Rev. B* **2010**, *81*, 165414.
- (72) Sanyal, B.; Eriksson, O.; Jansson, U.; Grennberg, H. Molecular adsorption in graphene with divacancy defects. *Phys. Rev. B* **2009**, *79*, 113409.

Supporting Information:

Understanding the Strength of the Selenium - Graphene Interfaces for Energy Storage Systems

Vidushi Sharma¹, David Mitlin^{2,*}, Dibakar Datta^{1,*},

¹Department of Mechanical and Industrial Engineering, New Jersey Institute of Technology, Newark, NJ 07103, USA

² Materials Science and Engineering Program & Texas Materials Institute, The University of Texas at Austin, Austin, TX, 78712-1591, USA

Corresponding Authors

*Email: dibakar.datta@njit.edu

*Email: david.mitlin@austin.utexas.edu

KEYWORDS: Density Functional Theory (DFT), Selenium, Graphene, Silicon, Interface, Charge Transfer, Density of States (DOS)

Section I. Energies of surface slabs for Se interface systems:

Work of separation is calculated from surface energies of material slabs (E_1 and E_2) and interface system energies (E_{12}). For surface energy calculation, optimized a-Se, c-Se, Gr and Al material slabs with an added vacuum of 12 Å in z dimensions were subjected to DFT. For calculation of interface system energies, the two materials were interfaced and a vacuum of 14Å was added in z-dimensions (normal to free surface). The presence of vacuum allows ions to undergo complete relaxation and prevent periodic influences. Table S1 shows final energies of the vacuum slabs which are used to determine interface strength of Se interfaces via work of separation. Details of work of separation of a-Si/Gr interface system were reported previously¹.

Table S1 Final energies and equilibrium dimensions of Se interfaces. For each interface system, E_1 is energy of slab 1 of substrate, E_2 is energy of slab 2 active electrode, E_{12} is the total energy of interface system as slab 3, and A is the area of contact at the interface.

S.	Interface	DFT optimized energy (eV)			Area (Ų)
no.	system	$\mathbf{E_1}$	$\mathbf{E_2}$	$\mathbf{E_{12}}$	
(i)	a-Se/Gr	-870.177	-94.16146	-970.5632	285.1462
(ii)	c-Se/Gr	-870.17899	-106.32525	-969.91917	285.1632
(iii)	c-Se/Al	-249.09390	-106.3577	-371.6000	260.984

Section II. Variation in graphene interface strength as Li concentration varies:

The interface strength value between active electrode and graphene is expected to decrease with increasing concentration of Li in the electrode. To validate this, interface strength between lithiated Si electrode and graphene substrate was calculated as described in Section I and compared with Si/Gr interface strength determined earlier. For creation of Li_{0.5}Si/Gr system, 32 Li atoms were sequentially inserted into *a*-Si₆₄/Gr as system was allowed to relax using ab-initio molecular dynamics (AIMD) simulations within the DFT framework of VASP. AIMD simulation permitted atoms to mix sufficiently. The simulation was run with 1 fs time interval at room temperature within NVT ensemble and 2 X 2 X 1 gamma centered k-meshes were taken into account. Post this, 3 material slabs were created of Gr, Li_{0.5}Si and Li_{0.5}Si/Gr interface with an added vacuum of 14 Å in z dimensions. The structures were optimized using DFT in VASP with configurations as described in the main manuscript. Figure S1 below shows interface strength for *a*-Si/Gr electrode reduces as the Li concentration is increased. The interface strength of Li_{0.5}Si/Gr interface was calculated to be 0.38 J/m² using equation 1 of work of separation (W_{sep}) from the main manuscript. Likeliness between Si/Gr and Se/Gr interfaces suggests interface adhesion at Se electrode and Gr interface will also decrease with increase in Li concentration.

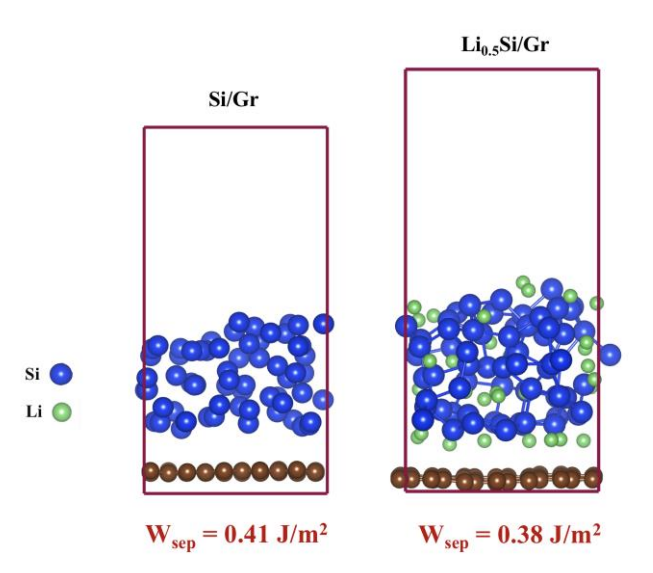


Figure S1 Drop in interface strength of graphene (Gr) with amorphous Si electrode as Li concentration increased in the system. Interface strength is determined as work of separation (W_{sep}) for Si/Gr interface to be 0.41 J/m² and Li_{0.5}Si/Gr to be 0.38 J/m².

Section III. Distortions in Se crystal in c-Se/Gr interface:

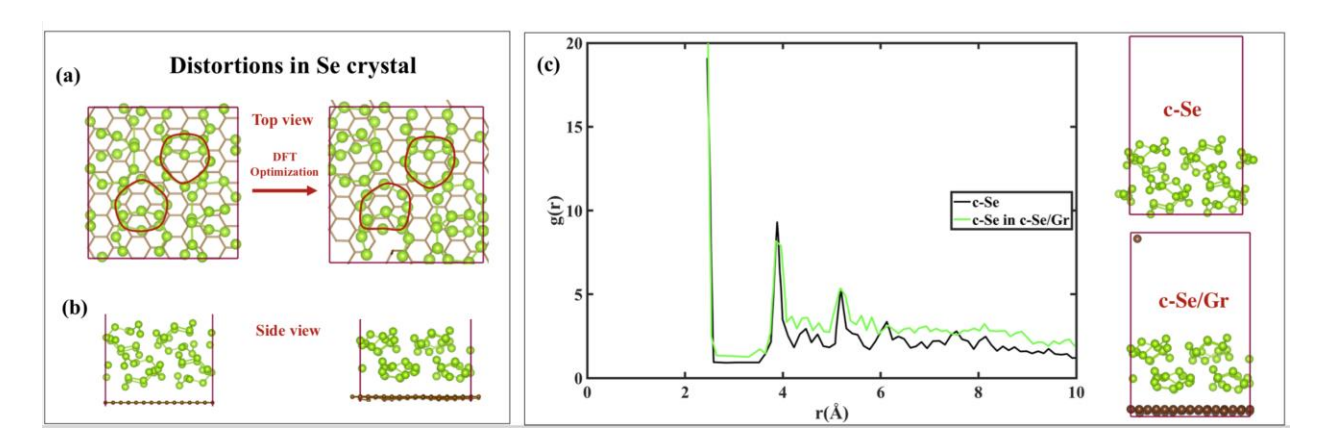


Figure S2 (a-b) Top and side view of initial and final DFT optimized structure of c-Se₆₄ over graphene substrate. Se atom rings of 8 were maintained with slight change in vertical orientations. The crystal structure condensed towards graphene causing changes in dihedral angles. **(c)** Comparative RDF plot of independent c-Se and c-Se optimized over graphene surface. No significant change in near neighboring distances or position of crystal peaks is noted in latter. Only the intensity of intermittent small peaks increases slightly with peak broadening.

Section IV. Planar averaged potential in *c*-Se/Al interface system:

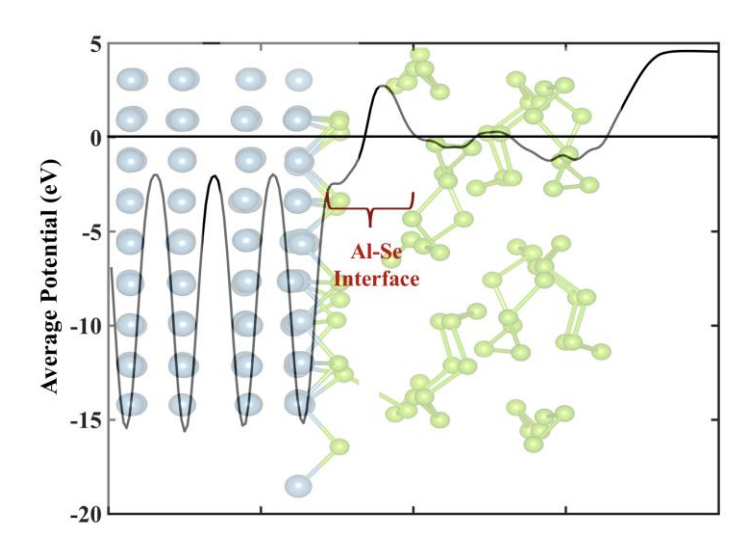


Figure S3 Planar average potential curves at Al and crystalline Se interface. An additional potential well of ~ -2.7eV is noted next to Al due to formation of Aluminum selenides on Al surface. Se-Se bonds on the Se surface break in the interfacial region leading to this surface reaction.

Section V. Surface energies of Selenium structures:

Surface energies of Se structures were determine as:

$$\frac{1}{A}\left(\mathbf{E}_{\mathrm{slab}}-n\mathbf{E}_{\mathrm{bulk}}\right)$$

Here, E_{slab} is the energy of Se vacuum slab, E_{bulk} is the energy of periodic Se bulk, n is the number of surfaces in slab and A is surface area of slab. The surface energies of selenium models are presented in Table S2. Surface energy of crystalline c-Se₆₄ is noted to be close to the experimental measure² of solid Se surface energy. With particle size, surface energy changes by $\sim 0.02 \text{ J/m}^2$ as noted for c-Se₆₄ and c-Se₃₂ in table S2.

Table S2 Surface energies of Selenium models in the present study.

Selenium model	Surface Energy (J/m²)
<i>c</i> -Se ₃₂	0.224
c-Se ₆₄	0.248
a-Se ₆₄	0.375

References

- 1. Basu, S.; Suresh, S.; Ghatak, K.; Bartolucci, S. F.; Gupta, T.; Hundekar, P.; Kumar, R.; Lu, T.-M.; Datta, D.; Shi, Y., Utilizing van der Waals slippery interfaces to enhance the electrochemical stability of Silicon film anodes in Lithium-ion batteries. *ACS applied materials & interfaces* **2018**.
- 2. Guisbiers, G.; Arscott, S.; Snyders, R., An accurate determination of the surface energy of solid selenium. *Applied Physics Letters* **2012**, *101* (23), 231606.